Optimizing Disordered Rock Salt Cathodes by Solid-State Synthesis and Design of Experiments for Enhanced Battery Performance

Eduardo C. M. Barbosa, Jianxuan Du, Avnish Singh Pal, Aleksandr Kondrakov,* and Torsten Brezesinski*

Aiming at discovering new positive electrode materials with superior electrochemical performance for application in lithium-ion batteries, this work focuses on the design of fluorine-free, manganese-rich disordered rock salt (DRX) cathodes. Samples with a starting composition of $Li_{1.1}Mn_{0.8}Ti_{0.1}O_2$ are successfully prepared by facile solid-state synthesis and further optimized through a design of experiments approach. Several key factors are examined, including carbon type and content as well as lithium (precursor) excess. The tailored DRX/carbon composites, using either graphite or multiwalled nanotubes, are capable of delivering specific capacities of up to 190 mAh g^{-1} and exhibit high cycling stability, with the capacity retention being greater than 90% after 100 cycles. This study emphasizes the importance of screening key factors in developing next-generation battery materials.

1. Introduction

In the search for sustainable energy solutions, the need to develop high-performance electrochemical storage systems remains essential.[1] Among the numerous cathode candidates within this field, disordered rock salt (DRX) materials have emerged as particularly promising owing to their high specific capacity, making them attractive for application in energy-dense Li-ion batteries (LIBs).[2–6] In addition, the utilization of such materials provides an environmentally conscious alternative to layered Ni-rich oxide cathodes by incorporating more abundant elements, thereby reducing the cost associated with the production of critical components.[2,3,7]

DRX materials are characterized by unconventional atomic arrangements that deviate from the typical long-range order observed in crystalline phases.[5,6,8] They often contain high-valence transition metal species, such as Ti^{4+}, Zr^{4+}, Nb^{5+}, or Mo^{6+}, to compensate for the charge introduced by the excess lithium and stabilize the site distortion caused by the (cation) disordering.[9–13] These d^0 transition metals improve mechanical stability, which ultimately enhances the cycling performance.[11,13–15]

Fluorination, enabled by the (cation) disordered nature of DRX materials, is a widely used strategy to increase lithium content and improve electrochemical stability.[7] However, in DRX systems, fluorine tends to attract lithium, forming localized Li-rich F environments that strongly influence the short-range order (SRO) within the material.[4,16] Other than the assumption of random distribution of cations, SRO represents their local arrangement, which directly affects the ion percolation channels.[15,17–19] While increasing fluorine content can connect isolated, Li-rich F clusters to form a well-connected Li$^+$ percolation network,[3] the solubility limit of fluorine poses a challenge. To achieve F-rich compositions, energy-intensive mechanochemical methods are often required to stabilize metastable phases.[7,8] In addition, the preference for F-free materials in electrochemical energy storage systems has gained momentum, primarily due to environmental and safety concerns associated with fluorinated compounds.[20–22] It should be noted though that F-free DRX cathodes may experience reduced capacity and faster degradation.[23–25]

To address the challenges associated with fluorination, such as the aforementioned lithium-attracting effect and the complexity it introduces into the synthesis process, this study employs solid-state synthesis for the fabrication of F-free DRX materials. This method not only simplifies the synthesis pathway, but also offers a more energy- and cost-efficient alternative with strong potential for scalability,

E. C. M. Barbosa, J. Du, A. S. Pal, A. Kondrakov, T. Brezesinski
Battery and Electrochemistry Laboratory (BELLA)
Institute of Nanotechnology
Karlsruhe Institute of Technology (KIT)
Kaiserstr. 12, 76131 Karlsruhe, Germany
E-mail: aleksandr.kondrakov@basf.com; torsten.brezesinski@kit.edu
A. S. Pal
Karlsruhe Nano Micro Facility (KNMFi)
Karlsruhe Institute of Technology (KIT)
Kaiserstr. 12, 76131 Karlsruhe, Germany
A. Kondrakov
BASF SE
Carl-Bosch-Str. 38, 67056 Ludwigshafen, Germany

ADVANCED
SCIENCE NEWS

www.advancedsciencenews.com

ADVANCED
SUSTAINABLE
SYSTEMS

www.advsustainsys.com

in line with the need to translate laboratory advances into industrially viable solutions for next-generation battery technologies.

Manganese, with its diverse oxidation states, stands out as a versatile redox-active species among the transition metals. Its capability to undergo reversible reactions while accommodating lithium renders it an ideal candidate for high-capacity cathode active materials (CAMs).[2,8,26,27] Aside from exhibiting promising charge-storage properties, Mn-based cathodes are capable of significantly enhancing the stability and safety of LIBs. Moreover, the abundance and economic viability of manganese make it a compelling choice for commercial applications, facilitating widespread adoption of advanced energy storage solutions that are crucial to meeting the world's increasing energy demands.[28,29]

This study focuses on exploring the potential of F-free DRX CAMs containing lithium, manganese, and titanium. By employing a reduced design of experiments (DOE) in the synthesis methodology, our objective is to maximize cyclability while attempting to understand the underlying principles governing the electrochemical behavior (redox activity).

2. Experimental Section

2.1. Synthesis

The DRX materials [with target/starting composition of $Li_{1.1}Mn_{0.8}Ti_{0.1}O_2$ (LMTO)] were synthesized by a two-step procedure. Initially, TiO_2 (anatase, 99.8%; Sigma-Aldrich), $LiOH \cdot H_2O$ (BASF SE), and Mn_2O_3 (98%; Thermo Fisher Scientific) were ground together under Ar atmosphere in a 125 mL glass jar. The mass of Mn_2O_3 and TiO_2 was maintained at 14.72 and 1.83 g, respectively, while that of $LiOH \cdot H_2O$ varied as follows: 11.71 g for 10% excess, 14.91 g for 40% excess, and 17.04 g for 60% excess. The powders were weighed and sealed in an Ar-filled glovebox with $[O_2]$ and $[H_2O] < 0.5$ ppm (MBRAUN), followed by grinding using a Kinematica laboratory blender (MICROTRON MB 550) at power setting 6 for 10 min. Subsequently, the mixtures were transferred to an alumina crucible, compacted by hand pressing, and quickly put into a tube furnace. Calcination was performed under Ar atmosphere at a heating rate of 10 °C min^{-1} from room temperature to 960 °C, with a dwell time of 2 h. Finally, the quartz tube was removed from the furnace to rapidly cool the materials.

2.2. Processing

The samples were hand ground and sieved using a 32 μm stainless-steel sieve. To further decrease particle size, they were ball milled. Typically, 1.6 g of sieved powder was placed in an 80 mL ZrO_2 jar containing 64 g of 3 mm diameter ZrO_2 balls. The latter step was performed in an Ar-filled glovebox to avoid air exposure during post-treatment. The jar was sealed, and the material was then milled at 1000 rpm for 3 min, followed by 600 rpm for 3 min, and 1000 rpm for another 3 min, in a planetary ball mill (PULVERISETTE 7; FRITSCH).

Table 1. Experimental design employed for optimizing slurry and cathode preparation.

Exp.	DRX	Carbon [wt%]	Carbon type
DOE01	LMTOe10	20	Graphite
DOE02	LMTOe60	15	Super 65
DOE03	LMTOe60	10	Graphite
DOE04	LMTOe40	15	Graphite
DOE05	LMTOe60	20	Nanotubes
DOE06	LMTOe40	10	Nanotubes
DOE07	LMTOe40	20	Super 65
DOE08	LMTOe10	15	Nanotubes
DOE09	LMTOe10	10	Super 65
DOE10	LMTOe40	20	Nanotubes
DOE11	LMTOe10	20	Nanotubes
DOE12	LMTOe40	10	Super 65

2.3. Design of Experiments

The experimental design employed a Taguchi partial factorial design, an efficient tool for the investigation of multiple factors with a relatively limited number of experimental runs. This method allows for the evaluation of factors influencing the performance of CAM, enabling the identification of optimal conditions while minimizing cost and time. The initial phase of the study comprised 9 individual experiments, which were subsequently augmented by three additional experiments based on the results to enhance the data treatment (see **Table 1**). The design included the following factors: $LiOH \cdot H_2O$ excess (treated as continuous but implemented with discrete levels of 10, 40, and 60%; the corresponding samples are referred to as LMTOe10, LMTOe40, and LMTOe60, respectively), carbon weight percentage (treated as continuous but implemented with discrete levels of 10, 15, and 20 wt%), and carbon type (a categorical factor with levels of "Graphite", "Super C65" [Imerys Graphite & Carbon], and "Nanotubes" [multi-walled, 6–9 nm × 5 μm, >95%; Sigma-Aldrich]). Moreover, the average density of the cathodes was used as a cofactor, dependent on the outcome for each material. The response variables, namely first-cycle discharge capacity and capacity retention after 50 and 75 cycles, were treated separately, with each variable weighted by the standard deviation derived from three measurements.

Stepwise regression was employed to iteratively refine the model by including or excluding factors based on their p-values and minimizing the Bayesian Information Criterion (BIC). Factors with p-values exceeding 0.05 were excluded, and the model exhibiting the lowest BIC was selected. Subsequently, the backward elimination was applied to remove factors with lower levels of statistical significance, ensuring that only the most relevant variables were retained in the final model. The assumption of homoscedasticity was validated by examining the residuals, which were found to be randomly distributed around zero, confirming variance consistency. Other assumptions, such as residual normality, were not explicitly tested, as the primary focus was on model fit and variance stability.

**ADVANCED
SCIENCE NEWS**

www.advancedsciencenews.com

**ADVANCED
SUSTAINABLE
SYSTEMS**

www.advsustainsys.com

Each experiment was performed three times to ensure reliability and reproducibility of results. To minimize variability, all cells were prepared and tested simultaneously under identical conditions to maintain consistency across experiments. Data analysis was performed using JMP 17.0.0, with model fitting performed using the Fit Model function. Standard least-squares regression with effect screening was used to assess the significance of each factor. Stepwise regression was used for factor selection, and BIC was used to determine the best model.

2.4. Blending with Carbon and CAM Washing

After the initial ball-milling step, the samples were combined with different amounts of carbon additives, according to the DOE conditions. The jar was sealed again, and the powder mixtures were milled at 300 rpm for 1 h. Following the carbon addition, each material underwent a washing procedure. To this end, 1.5 g of CAM was washed using DI water in a 1:5 weight ratio in a round-bottom flask containing a stir bar. Specifically, the samples were left stirring overnight, then centrifuged, washed once with DI water and once with ethanol, and finally dried in a vacuum oven (BINDER) at 60 °C. Next, post-treatment at 100 °C for 2 h under dynamic vacuum was performed to ensure complete water removal and enhance contact between the CAM and the carbon particles. Finally, the composite materials were heated at 300 °C for 12 h under dynamic vacuum using a glass oven (Büchi), followed by sieving to less than 32 μm.

2.5. Slurry and Electrode Preparation

Cathode slurries were prepared by blending the DRX/carbon composites with *N*-methyl-2-pyrrolidone (NMP, ≥99.5%; Merck KGaA) at 2000 rpm for 3 min, followed by another 3 min at 400 rpm, using a planetary centrifugal mixer (Thinky ARE-250). After the initial mixing step, a 7.5 wt% binder solution of polyvinylidene difluoride (PVDF, Solef 5130; Solvay) in NMP was added to the slurry in the mixing cup. The binder content was maintained at 5 wt% in all cases, while the carbon content varied according to the DOE conditions. Next, the mixture was treated again at 2000 and 400 rpm for 3 min each to produce a uniform slurry. Using a motorized film applicator (ERICHSEN COATMASTER 510), the slurry was immediately applied to a 0.03 mm-thick Al foil (200 μm slit size), leading to areal loadings of 2–6 mg_{CAM} cm^{-2}. The resulting cathodes were first dried at room temperature, and then they were held overnight at 120 °C under dynamic vacuum. All materials were cast in a dry room with a dew point of lower than −50 °C.

2.6. Coin-Cell Assembly

The cathodes were calendered at room temperature and at 14 N mm^{-1} and then cut into 13 mm diameter electrodes. CR2032 coin cells were assembled in an Ar-filled glovebox and comprised the cathode, a GF/A glass microfiber separator (17 mm diameter, 0.25 mm thickness; Whatman), a Li-metal anode (15 mm diameter, 1.0 mm thickness), and 95 μL of electrolyte (1.0 M $LiPF_6$ in fluoroethylene carbonate and diethyl carbonate, 2:8 by weight).

2.7. Electrochemical Testing

In general, at least three independent cells were cycled for each experiment, and the results are presented as the average of these measurements. They were cycled in a potential window of 2.5–4.5 V versus Li^+/Li at 25 °C, with a constant voltage step at 4.5 V (either for 1 h or until the current dropped below C/50), using a battery test system (MACCOR Inc.). After assembly and 2 h of open-circuit voltage (OCV) resting, electrochemical testing was done by two cycles of galvanostatic cycling at C/10 (with 1C = 200 mA g_{CAM}^{-1}), followed by long-term cycling at C/3, with rate capability testing at C/2, 1C, 2C, and 3C discharge (with C/3 charge) for two cycles each after 12 cycles.

2.8. X-Ray Diffraction (XRD)

A STADI-P diffractometer (STOE) equipped with a Mo anode (λ = 0.70932 Å) and a MYTHEN 1K strip detector (DECTRIS) was employed to acquire XRD patterns of the samples in Debye–Scherrer geometry. The integration time was set to 14 h, with 2θ ranging from 5 to 50°. Samples were prepared by packing the sieved materials in 0.5 mm diameter quartz capillaries. Rietveld refinement analyses were performed using GSAS-II software.

2.9. Inductively Coupled Plasma-Optical Emission Spectroscopy (ICP-OES)

The metal contents were determined by ICP-OES using an iCAP 7600 DUO (Thermo Fisher Scientific). Samples were analyzed after acid digestion in a DAB-2 pressure-temperature digestion system.

2.10. Electron Microscopy

Scanning electron microscopy (SEM) measurements were performed on a LEO 1530 microscope (Zeiss) at 10 kV. Samples were prepared by dry casting the powders onto carbon tape, followed by thoroughly "cleaning" with compressed nitrogen gas to remove unsupported debris.

Transmission electron microscopy (TEM) was performed using an aberration-corrected microscope (Themis Z; Thermo Fisher Scientific) at an operating voltage of 300 kV. Samples were prepared by dry casting the powders onto plasma-cleaned (50% Ar + 50% O_2 at 40% power), carbon-coated gold grids.

3. Results and Discussion

The synthesis of DRX materials presented here involved an incremental excess of LiOH•H_2O. The initial synthesis targeted the $Li_{1.1}Mn_{0.8}Ti_{0.1}O_2$ stoichiometry, employing a 10% LiOH•H_2O excess (LMTOe10, based on x = 1.1), to account for lithium losses during processing. Consequently, two additional samples were prepared by increasing the excess to 40 and 60%, referred to as LMTOe40 and LMTOe60, respectively. In particular, a solid-state synthesis approach was employed, whereby each material was
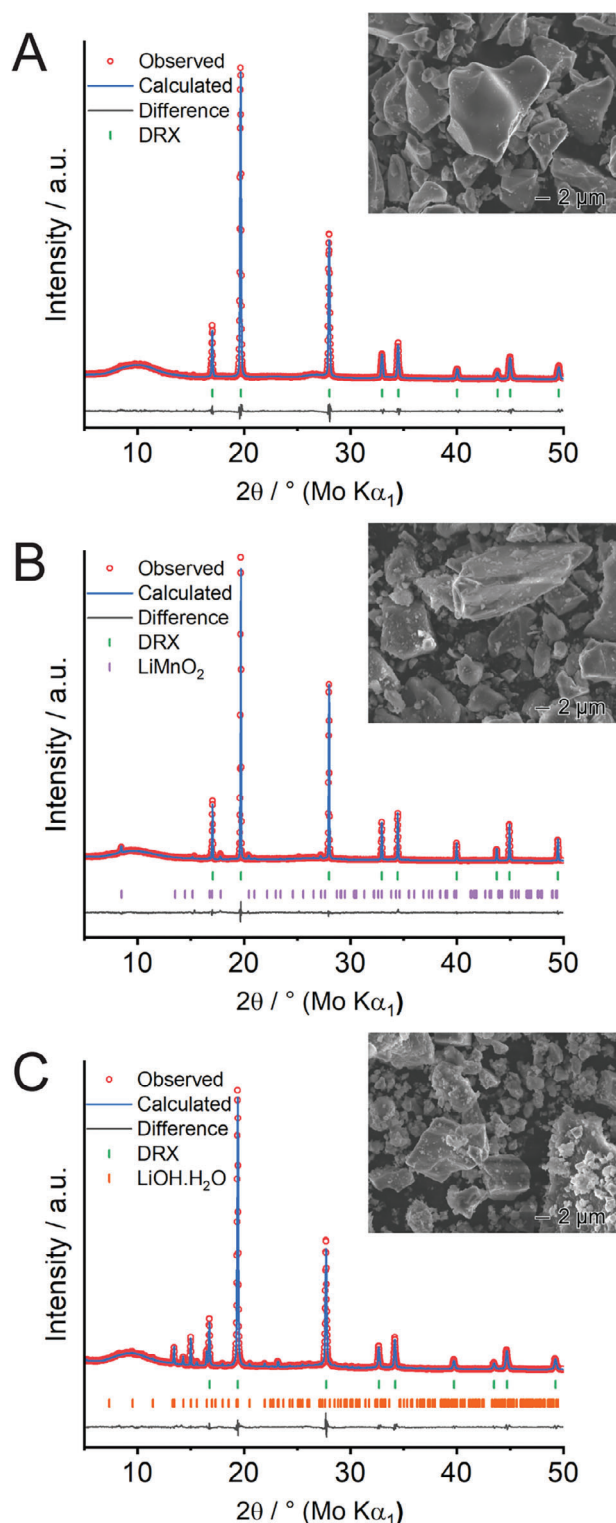
**ADVANCED
SCIENCE NEWS**

www.advancedsciencenews.com

**ADVANCED
SUSTAINABLE
SYSTEMS**

www.advsustainsys.com

Figure 1. Structural and morphological characterizations of the pristine samples prepared with A) 10% (LMTOe10), B) 40% (LMTOe40), and C) 60% LiOH•H$_2$O excess (LMTOe60). The observed, calculated, and difference profiles are shown as red circles, blue lines, and black lines, respectively. Vertical marks indicate the expected Bragg positions. Corresponding SEM images are shown in the insets.

Table 2. Stoichiometries based on ICP-OES analysis and structural refinement results.

Sample	Formula	DRX [wt%]	a [Å]	R_{wp} [%]
LMTOe10	$Li_{1.18}Mn_{0.82}Ti_{0.09}O_2$	100.0	4.152(1)	6.71
LMTOe40	$Li_{1.38}Mn_{0.76}Ti_{0.09}O_2$	97.1	4.149(6)	5.37
LMTOe60	$Li_{1.42}Mn_{0.76}Ti_{0.08}O_2$	91.6	4.179(8)	5.98

produced without the need for ball milling. Specifically, the materials were produced by blending the precursors in a laboratory mixer, followed by high-temperature calcination in a less than 4 h procedure, yielding more than 90% of the desired DRX phase, as determined by Rietveld refinement of X-ray diffraction (XRD) data (see **Figure 1A–C**). Rapid cooling to keep lithium losses through evaporation at a minimum was accomplished by removing the quartz tube containing the samples from the furnace as soon as the thermal treatment was concluded. The use of excess lithium in the synthesis was intended to achieve the formation of a percolation network within the CAMs, thereby enhancing battery performance.[5,6,30] The molecular formula (composition) for each material in the pristine state (prior to washing) employed in this work, as determined by inductively coupled plasma-optical emission spectroscopy (ICP-OES), as well as the corresponding weight percentage of DRX phase, refined lattice parameter, and weighted profile residual factor from Rietveld analysis are given in **Table 2**.

ICP-OES analysis revealed a significant difference between LMTOe10 and the other two samples. LMTOe10 exhibited a stoichiometry that was closest to the target composition and further had the highest DRX phase fraction. Both LMTOe40 and LMTOe60 had similar stoichiometries, differing primarily in sample purity. Rietveld refinements confirmed the presence of the DRX phase, with Li, Mn, and Ti occupying the 4a sites, while O is situated on the 4b sites. Further details can be found in the Supporting Information (see Tables S1–S3).

The LMTOe10 sample clearly displayed the presence of DRX, with no additional reflections indicating the formation of side phases (see Figure 1A). However, the LMTOe40 sample exhibited LiMnO$_2$ as an impurity phase, as shown in Figure 1B, suggesting that higher temperatures and/or longer reaction times may be necessary to achieve full conversion. Conversely, the LMTOe60 sample had a composition comparable to that of LMTOe40, without the aforementioned impurity (see Figure 1C). This indicates that the lithium incorporation reached its saturation point, with the remainder vaporizing (to some extent) due to the high calcination temperature. It should also be noted that LMTOe60 exhibits some LiOH (Li$_2$O) impurities, further corroborating the conclusion that the solubility limit had already been reached with the aforementioned samples. Although Rietveld refinements were successfully performed for the major phases, additional features were observed in the XRD patterns. These include broad and low-intensity reflections centered around 10 and 26° 2θ, which have been previously explored and apparently can be attributed to the SRO in these materials.[15,16,31,32]

Scanning electron microscopy (SEM) images (see insets in Figure 1A–C) demonstrate that all three samples contain particles of diameters ranging between 100 nm to ≈10 μm. As evident,

**ADVANCED
SCIENCE NEWS**

www.advancedsciencenews.com

**ADVANCED
SUSTAINABLE
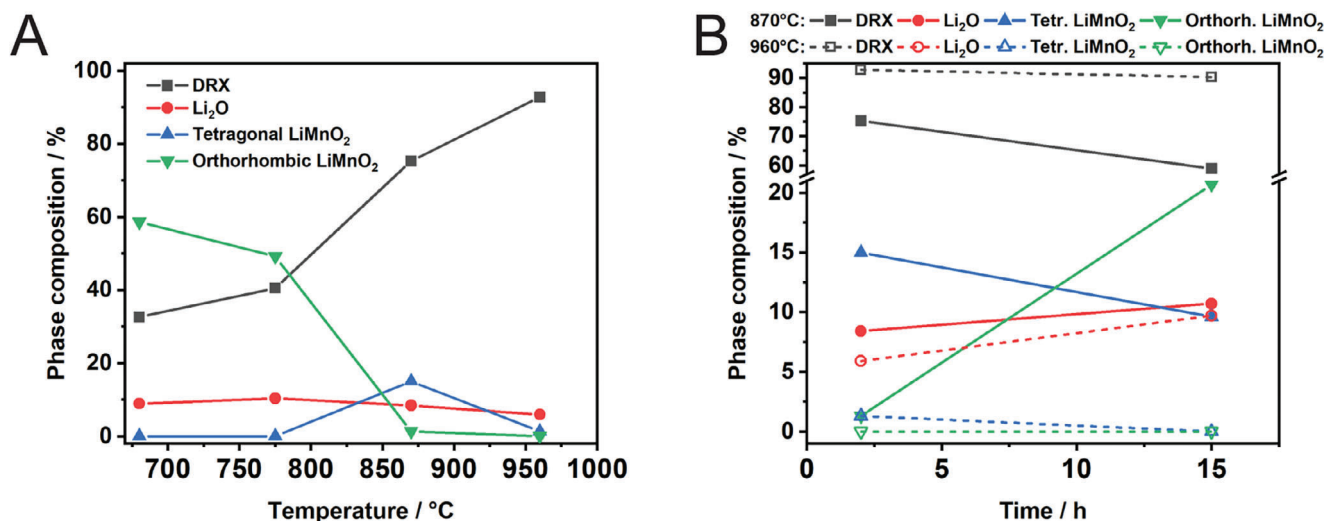SYSTEMS**

www.advsustainsys.com

Figure 2. Phase composition of the pristine samples prepared with 60% LiOH•H$_2$O excess (LMTOe60). Results from Rietveld analysis of XRD data collected from materials synthesized A) at different temperatures (with 2 h dwell time) and B) at 870 and 960 °C with dwell times of 2 and 15 h.

LMTOe10 exhibits particles with sharp edges and rounded and flat surfaces. In contrast, the LMTOe40 and LMTOe60 samples have comparable morphologies, but with augmented surface irregularities, which are most pronounced for LMTOe60. This can be explained by the different levels of impurities found in these materials.

To better understand the DRX phase formation, the synthesis was performed at different temperatures while keeping the rest of the procedure the same. Specifically, the LMTOe60 composition was selected to examine the likelihood of LiOH•H$_2$O excess producing either LiMnO$_2$, as observed for LMTOe40, or Li$_2$O, as observed for LMTOe60. XRD indicated that the DRX phase begins to form at temperatures as low as 680 °C (see **Figure 2A**), with a prominent orthorhombic LiMnO$_2$ (o-LiMnO$_2$) phase being present. As the temperature increases, the orthorhombic phase is converted into the DRX. At temperatures exceeding about 850 °C, the o-LiMnO$_2$ transforms into the tetragonal LiMnO$_2$ (t-LiMnO$_2$) phase. In contrast, when similar experiments are performed with a dwell time of 15 h, as shown in Figure 2B, both DRX and t-LiMnO$_2$ are found to convert back into the o-LiMnO$_2$ phase at about 870 °C. This indicates that longer reaction times at "non-ideal" calcination temperatures offer sufficient energy for structural rearrangements, suggesting preferential formation of layered o-LiMnO$_2$ over t-LiMnO$_2$. Conversely, at 960 °C, increasing reaction times primarily affect the Li$_2$O fraction.

The materials studied here required further processing to be employed as CAMs. Compared to other studies available in the literature, the main difference appears to be the particle size. Samples synthesized by ball-milling techniques typically produce particles of sizes ranging from 100 to 600 nm, whereas herein the particle sizes reached up to several microns in diameter.[2,5,13,14,33] Because decreasing the size directly reduces the percolation path length for charge transport, the materials also underwent a short-term, high-energy ball-milling step, followed by lower-energy milling in the presence of carbon to facilitate enhanced contact between the DRX and the conductive additive particles.[34–37] Due

to the use of LiOH•H$_2$O excess in the synthesis, especially in the case of LMTOe40 and LMTOe60, all samples were subjected to washing prior to electrode preparation and electrochemical testing.

As the samples were mixed with different types and amounts of carbon additives prior to the washing step, post-washing ICP-OES analysis did not provide directly comparable results. However, the results of selected samples indicate that the influence of LiOH•H$_2$O excess on the Li content in the DRX materials is less pronounced than initially assumed. In addition, variations in LiOH•H$_2$O excess appear to subtly alter the Mn/Ti ratio, although the nominal ratios were consistent across the samples. This observation is reasonable given the difficulty in verifying the presence of oxygen vacancies that could accommodate the additional charge introduced by Li excess in DRX materials. Despite these smaller-than-expected differences, the samples were considered suitable for inclusion in the DOE, where LiOH•H$_2$O excess served as one of the categorical factors in the experimental design.

To gain insight into the effects that the conductive additive and CAM have on the electrochemical performance, a reduced DOE was planned and implemented. This approach was employed (i) to tailor the slurry mixture and (ii) to verify the role of DRX composition. Three primary factors were selected for analysis, namely carbon content, carbon type, and LiOH•H$_2$O excess, each divided into three levels. A full factorial design examining all possible combinations of these factors would require 27 experiments. However, to optimize resources and time, an orthogonal array design (Taguchi method) was generated. This approach ensures that the selected experiments are statistically representative while reducing the total number. **Table 3** summarizes the experimental design and the resulting electrochemical performance metrics, including first-cycle specific discharge capacity at C/10 and capacity retention after 50 and 75 cycles at C/3 (relative to the first cycle after rate performance testing), referred to as CR$_{50}$ and CR$_{75}$, respectively. These metrics provide a comprehensive dataset for analyzing the influence of each factor on performance.

ADVANCED
SCIENCE NEWS

www.advancedsciencenews.com

ADVANCED
SUSTAINABLE
SYSTEMS

www.advsustainsys.com

Table 3. DOE results for the samples prepared with different LiOH•H$_2$O excesses and carbon contents and types.

Exp.	1st q_{dis} [mAh g$_{CAM}$$^{-1}$]	CR$_{50}$ [%]	CR$_{75}$ [%]
DOE01	144.7 ± 6.3	93.9 ± 1.7	89.8 ± 2.3
DOE02	115.7 ± 25.9	25.6 ± 26.8	18.6 ± 19.0
DOE03	118.9 ± 7.1	46.7 ± 17.1	38.7 ± 13.7
DOE04	171.6 ± 1.0	78.7 ± 4.7	70.6 ± 4.1
DOE05	172.6 ± 8.1	96.2 ± 2.2	95.6 ± 2.0
DOE06	193.6 ± 3.7	40.2 ± 6.7	30.7 ± 5.4
DOE07	146.9 ± 12.0	51.7 ± 13.1	45.4 ± 12.1
DOE08	155.5 ± 0.3	85.4 ± 1.4	71.9 ± 2.0
DOE09	2.4 ± 1.5	68.8 ± 22.5	61.6 ± 19.8
DOE10	181.8 ± 3.0	94.0 ± 2.3	90.8 ± 2.5
DOE11	156.2 ± 0.8	96.4 ± 1.6	94.4 ± 1.1
DOE12	3.4 ± 3.1	72.9 ± 24.0	65.3 ± 21.8

Initially, the DOE01 to DOE09 experiments were designed using the Taguchi method. Based on least-squares fitting of the discharge capacities and CR$_{50}$ data, DOE10 through DOE12 were then performed. These additional experiments targeted specific parameter combinations to refine the understanding of the response surface. The cycling data for the different cells can be found in Figure S1 (Supporting Information). **Figure 3** shows the effect of each of the three factors on first-cycle specific discharge capacity and CR$_{50}$. Each line represents the change in response factor as a single factor changes, while the effects of the other factors are averaged out. The slope of these lines provides an intuitive indication of how strongly each factor affects the response, with steeper slopes corresponding to greater influence. This type of plot is commonly referred to as a main effects plot in DOE. It is particularly useful for visualizing and interpreting the influence of independent variables on performance metrics, enabling the identification of the most critical factors for optimization. By isolating the effects of individual factors, the main effects plot provides a clearer understanding of the experimental system, even when there are interactions between factors. As a result of the exceptionally low average capacities achieved with DOE09 [(2.4 ± 1.5) mAh g$_{CAM}$$^{-1}$ in the initial cycle], this sample was excluded from the subsequent calculations.

In general, the results indicate that the samples containing Super C65 carbon black deliver lower capacities (DOE02, 07, 09, and 12) than the other cathodes and exhibit poor rate performance. Low Super C65 contents result in inefficient energy storage, as observed for DOE09 and 12. However, when the carbon content is increased, the DRX materials are capable of delivering some capacity (DOE02 and 07), but the capacity retention is unsatisfactory. Samples containing graphite (DOE01, 03, and 04) delivered higher initial specific discharge capacities, ranging from (118.9 ± 7.1) mAh g$_{CAM}$$^{-1}$ to (171.6 ± 1.0) mAh g$_{CAM}$$^{-1}$, with the capacity retention tending to increase with increasing carbon content. This suggests that these cathodes suffer from electrical (electronic) conductivity issues. The most favorable outcomes were achieved with the materials containing multiwalled carbon nanotubes (DOE05, 06, 08, 10, and 11). Still, the material blended with 10 wt% nanotubes (DOE06) only showed (40.2 ± 6.7)% ca-

pacity retention after 50 cycles, while samples having a higher carbon content demonstrated greater stability, as evidenced in DOE05, 08, 10, and 11, retaining (96.2 ± 2.2)%, (85.4 ± 1.4)%, (94.0 ± 2.3)%, and (96.4 ± 1.6)% of their capacity, respectively. This may be attributed to the combined effect of high specific surface area and electronic conductivity of carbon nanotubes. While graphite has the lowest specific surface area (≈3 m^2 g^{-1}), it also exhibits the highest conductivity (≈2100 S m^{-1}). The nanotubes exhibit the highest specific surface area (≈270 m^2 g^{-1}) and the lowest conductivity (≈540 S m^{-1}) among the additives tested here. By contrast, Super C65 has a specific surface area of ≈60 m^2 g^{-1} and a similar conductivity to that of the nanotubes. Of note, the latter conductivity values have been determined on powder samples compacted at 5 MPa, as detailed in the study by Marinho et al.[38]

Figure 4A,B shows the optimized regression models derived from the DOE results, plotted to identify the major factors influencing the observed responses. Upon completion of DOE10 to DOE12, a least-squares approach was applied to account for the main factors. For more accurate fitting of the initial capacities, the average electrode density was included in the regression model along with the factors of carbon type and carbon content. Similar to DOE09, DOE12 was identified as an outlier and therefore removed from the analysis to avoid biasing the results. The fitting process revealed clear influences of key variables. For the first-cycle specific discharge capacity (Figure 4A), average electrode density emerged as the most significant factor, with an inverse relationship to capacity. Carbon type and content also contributed to capacity, but to a lesser extent. In terms of capacity retention (Figure 4B), carbon content proved to be the dominant factor, with higher content positively correlating with improved retention. In addition, carbon type played an important role, with nanotubes and graphite providing better retention than Super C65, which had a negative effect. The numerical results of this analysis, including fitted coefficients and confidence intervals, are detailed in Figure S2 (Supporting Information). These results highlight the interplay between electrode composition and electrochemical performance and provide a more detailed understanding of the DRX system.

The primary electrochemical testing results for the samples containing either 20 wt% (DOE05, 10, and 11) or 10 wt% nanotubes (DOE06) are presented in **Figure 5A–F**. These materials exhibit similar first-cycle voltage profiles (see Figure 5A), with a capacity creep observed for those having 20 wt% nanotubes (see Figure 5B). This increase in capacity during the first few cycles could be associated with structural changes. Of note, recent results indicate that the presence of certain lithium manganates, which may form during cycling, can enhance the capacity of DRX cathodes.[6,39,40]

A clear distinction is evident with the incorporation of more carbon, with DOE06 showing inferior stability and rate capability. DOE10 delivered the highest specific discharge capacity of about 194 mAh g^{-1} following the initial increase (21st cycle, C/3, see Figure 5B). Thus, more detailed investigations were conducted on this system. Figure 5C shows the voltage profiles of the DOE10 cathode for cycles 3–12. As mentioned previously, a continuous increase in capacity was observed during these initial cycles at C/3 (corresponding to a specific current of 66.7 mA g^{-1}). This increase is clearly reflected in the voltage profiles, particularly at

**ADVANCED
SCIENCE NEWS**

www.advancedsciencenews.com

**ADVANCED
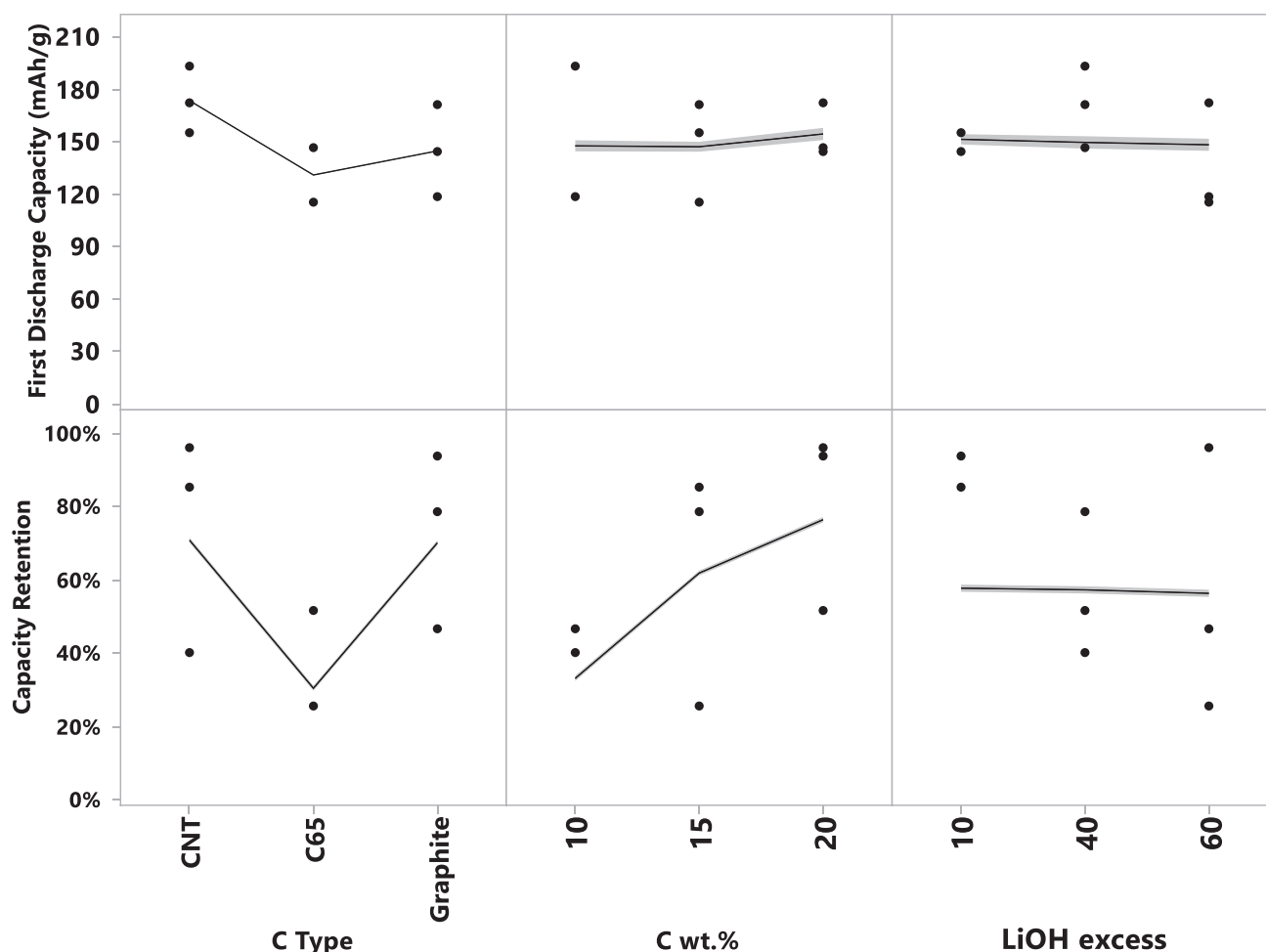SUSTAINABLE
SYSTEMS**

www.advsustainsys.com

Figure 3. Main effects plot of the DOE approach based on the first 9 experiments showing the influence of the three factors on first-cycle specific discharge capacity at C/10 and capacity retention after 50 cycles at C/3 (CR_{50}). Each data point represents the mean response for a given level of factor, averaged across all levels of the other factors. The slope of the lines indicates the magnitude of effect of the factor on each performance metric, with steeper slopes reflecting stronger effects. DOE09 was classified as an outlier and is not shown in these graphs.

about 4.1 and 2.9 V versus Li$^+$/Li upon charge and discharge, respectively. The feature at 2.9 V suggests a phase transition, which may correspond to the formation of a spinel-like phase. Further analysis, as discussed in the section on transmission electron microscopy (TEM) below, provided additional evidence supporting this interpretation. To verify the stability of this material, charge/discharge tests were also performed at higher current rates on discharge (see Figure 5D). However, no major differences in cyclability were observed, demonstrating its robustness under different conditions. Subsequently, an attempt was made to improve upon the capacity by changing the potential window from 2.5–4.5 to 2.0–4.5 and 1.5–4.8 V versus Li$^+$/Li. As can be seen from Figure 5E, in doing so, the material is in fact able to deliver much higher capacities (by a factor of up to 1.8) while sacrificing stability. According to literature reports, the reasons behind the accelerated fading are primarily irreversible oxidation of lattice oxygen at high potentials, causing structural degradation (surface densification, etc.), and electrochemical electrolyte decomposition at low potentials.[23,41,42] Consequently, similar profiles were found for the evolution of average discharge voltage

(see Figure 5F), with stable behavior only achieved for 2.5–4.5 V versus Li$^+$/Li.

Morphological and structural changes after 200 cycles at C/3 rate were also evaluated for the DOE10 sample. Specifically, they included alterations of the crystal structure. No major morphological differences were found by SEM (see **Figure 6A**). As expected, prior to cycling, the material was composed of DRX and (graphitic) carbon phases (see Figure 6B). After cycling, a distinct decrease in crystallite size was noted, accompanied by the formation of a new phase, as can be seen from the XRD patterns in Figure 6C. This agrees with the evolution of voltage profiles seen in Figure 5C. However, due to the limited data resolution, the new phase formed could not be reliably identified by Rietveld analysis.

To address this issue, TEM measurements were conducted on both the pre- and post-cycling sample (see below). In addition, the comparison of XRD patterns in Figure 6C reveals subtle peak shifts, suggesting some changes to the percolation network, which apparently negatively affect the electrochemical performance. Similar observations have been made in previous studies.[37,42]
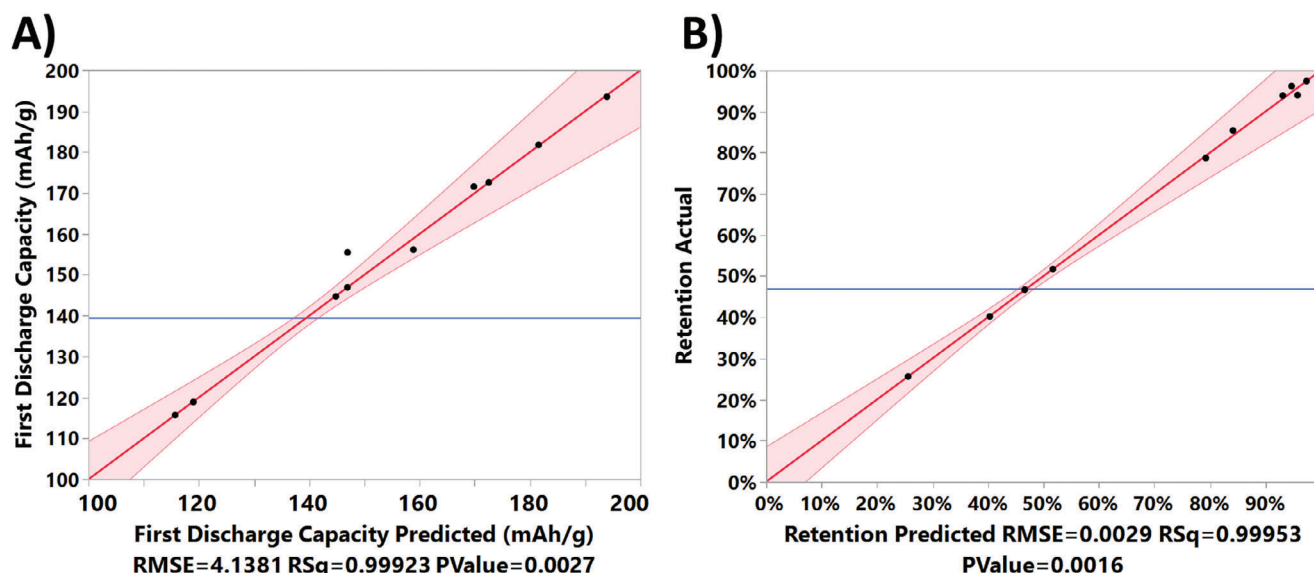
**ADVANCED
SCIENCE NEWS**

www.advancedsciencenews.com

**ADVANCED
SUSTAINABLE
SYSTEMS**

www.advsustainsys.com

Figure 4. Optimized fits of the DOE results shown as effects plots, where the response factors–first-cycle specific discharge capacity at C/10 and capacity retention after 50 cycles at C/3 (CR$_{50}$)–were separately modeled to evaluate the main contributing factors. DOE09 and DOE12 (outliers) were not considered in these calculations. A) First-cycle specific discharge capacity versus the carbon content, carbon type, LiOH•H$_2$O excess, and average electrode density. The blue line represents the null hypothesis (no factor influence), while the red line indicates the calculated model, with the shaded red area denoting the 95% confidence interval. B) Capacity retention versus the carbon content, carbon type, and LiOH•H$_2$O excess.

TEM was performed to examine the structural changes occurring during battery operation on the nanometer level. The bright-field image in **Figure 7A** depicts a mixture of DRX particles and carbon nanotubes (prior to cycling). Figure 7B presents the electron diffraction pattern collected from the area denoted by the blue circle in Figure 7A, indicating the presence of a rock salt phase of polycrystalline nature. To gain further insight into the crystal structure, a selected area electron diffraction (SAED) pattern was collected from a single particle (denoted by the red circle in Figure 7A). This pattern also refers to a single-phase rock salt with lattice parameter a_{RS} = 4.14 Å, as illustrated in Figure 7C. The prominent ring at 3.46 Å (d-spacing) can be attributed to the (002)$_{CNT}$ plane of the carbon nanotubes. Figure 7D shows a phase-contrast, high-resolution TEM (HRTEM) image of the same sample, with magnified views of the highlighted areas shown in Figure 7E,F. The fast Fourier transform (FFT) patterns from these areas indicate that the images were taken along [001] and [101] zone axes. The interplanar spacings match the rock salt phase mentioned previously.

To ascertain the nature of the structural changes induced by electrochemical cycling, a similar TEM investigation was conducted on the DOE10 sample after 200 cycles at C/3 rate. **Figure 8A** presents a bright-field image of the post-cycling material. The image clearly demonstrates the presence of nanoscale particles and carbon nanotubes. The SAED pattern collected from the area denoted by the blue circle in Figure 8A further corroborates the presence of a rock salt phase with similar lattice parameter to that observed for the pre-cycling sample (see Figure 8B). However, the electron diffraction pattern in Figure 8C indicates the presence of a mixed microstructure consisting of both rock salt and spinel phases. The innermost ring represents the (111)$_{Sp}$ d-spacing of about 4.82 Å of the spinel phase, while some of the diffraction rings, i.e., with d = 2.07 and 1.48 Å, can be

considered common for both the rock salt phase and the spinel phase along the (200)$_{RS}$/(400)$_{Sp}$ and (220)$_{RS}$/(440)$_{Sp}$ planes, respectively.

To further confirm spinel formation in the post-cycling sample, HRTEM imaging of a particle present in the area denoted by the red circle in Figure 8A was carried out. In fact, the image and corresponding FFT shown in Figure 8D provide profound evidence of the presence of a spinel phase with lattice parameter $a_{Sp} \approx 8.4$ Å, particularly so the intensity variations in the interference pattern along the [110] and [100] directions (marked by red arrows) and the d-spacings (marked by cyan lines). Our findings align well with recent studies on the formation of spinel-like δ-phases in DRX materials during electrochemical cycling, further corroborating the experimental findings.[40,43–45]

4. Conclusion

In this study, we established a solid-state synthesis route for Li-excess, Mn-rich cathodes and optimized their electrochemical performance using a DOE approach. LMTO DRX materials with different lithium (precursor) excesses were successfully prepared and employed in the fabrication of electrodes. The DOE approach facilitated efficient investigation of the effect of lithium (precursor) excess, as well as carbon additive type and content. The results demonstrate that incorporation of 20% carbon nanotubes leads to a notable enhancement in conductivity, accompanied by an increase in capacity and cycling stability. The DOE10 sample, comprising 40% lithium (precursor) excess and 20% carbon nanotubes, exhibits the best electrochemical performance, demonstrating good stability across a broad range of current rates. XRD and TEM analyses of this material indicate the formation of a spinel-like phase during battery operation, which is also evident from the cycling data.
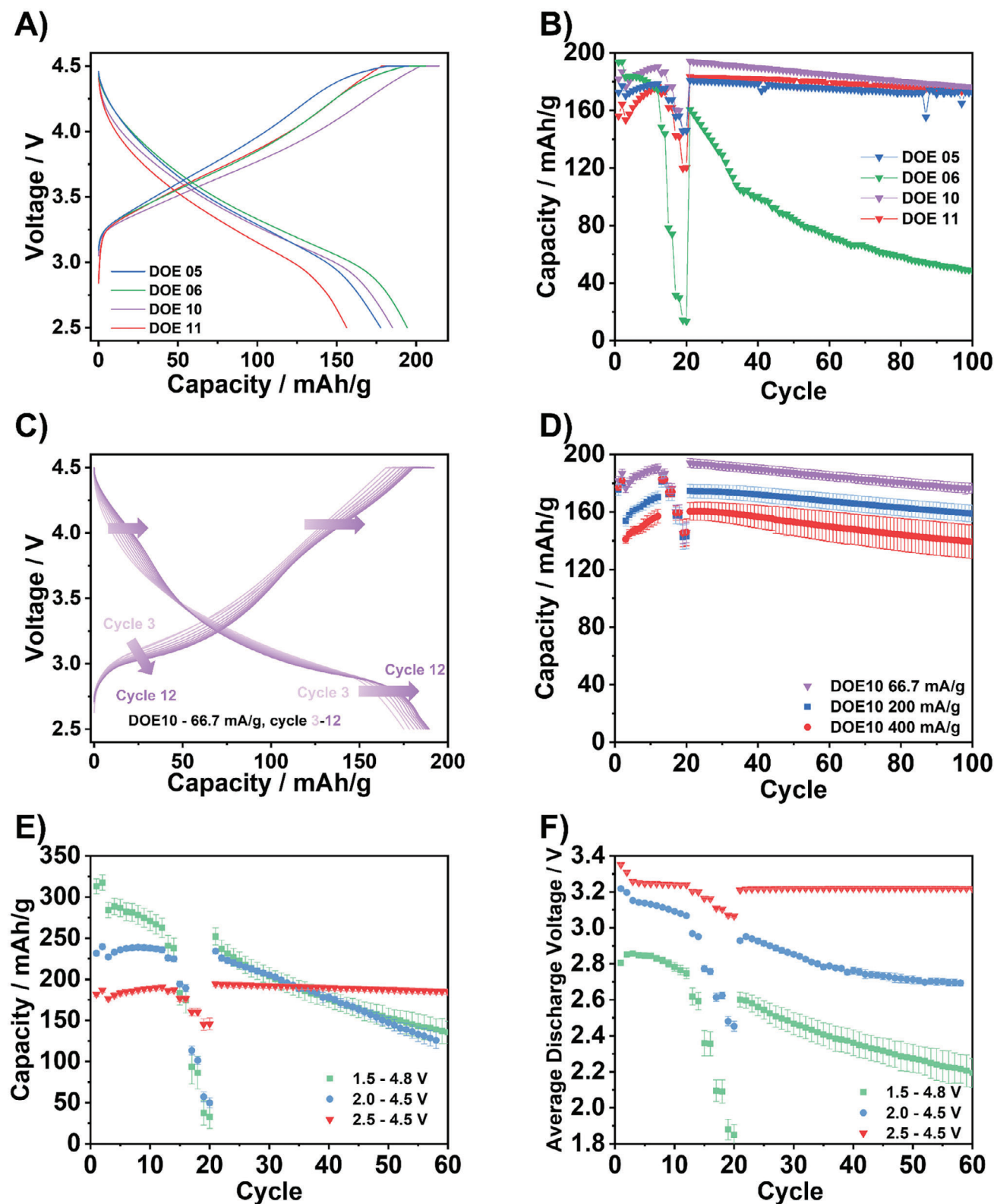
Figure 5. A) First-cycle charge/discharge profiles at C/10 of selected samples (with multiwalled carbon nanotubes) from the DOE study in a potential window of 2.5–4.5 V versus Li$^+$/Li and B) corresponding long-term cycling performances at C/3. C) Voltage profiles of DOE10 at C/3 for cycles 3–12. Cycling performance of DOE10 D) at different specific currents (corresponding to 1C and 2C, instead of C/3) and E) in different potential windows at C/3. F) Corresponding average discharge voltages. Note that the first two cycles were always performed at C/10 and that there was a rate performance test implemented after 12 cycles, with two cycles each at C/2, 1C, 2C, and 3C discharge.
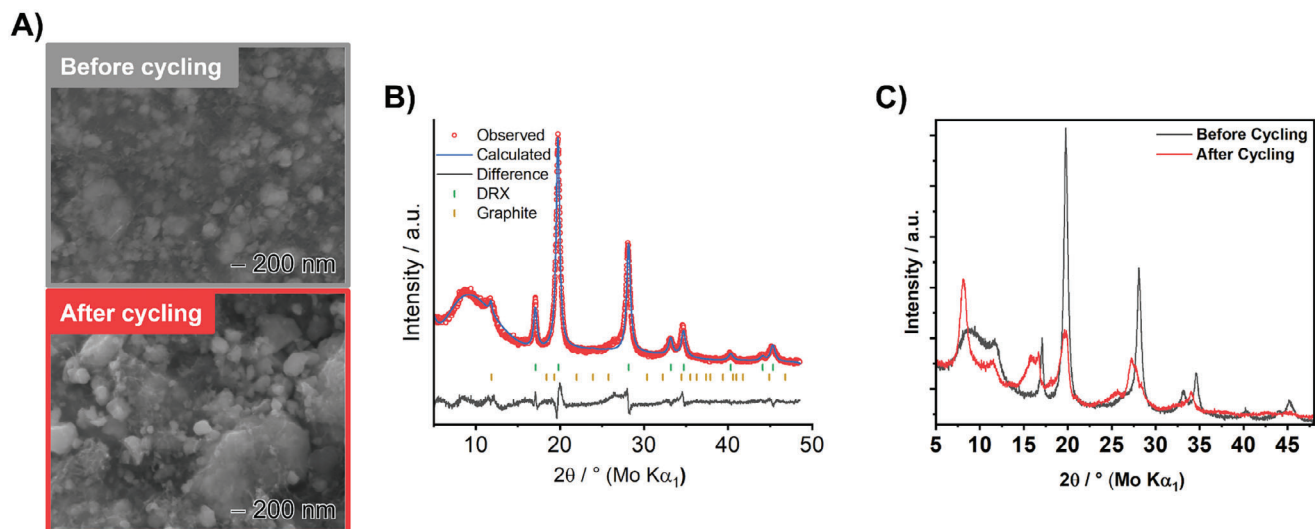
Figure 6. A) SEM images of the DOE10 sample taken before cycling and after 200 cycles at C/3 rate. B) Structural characterization prior to cycling. The observed, calculated, and difference profiles are shown as red circles, blue line, and black line, respectively. Vertical marks indicate the expected Bragg positions. C) Comparison of XRD patterns collected before and after cycling.
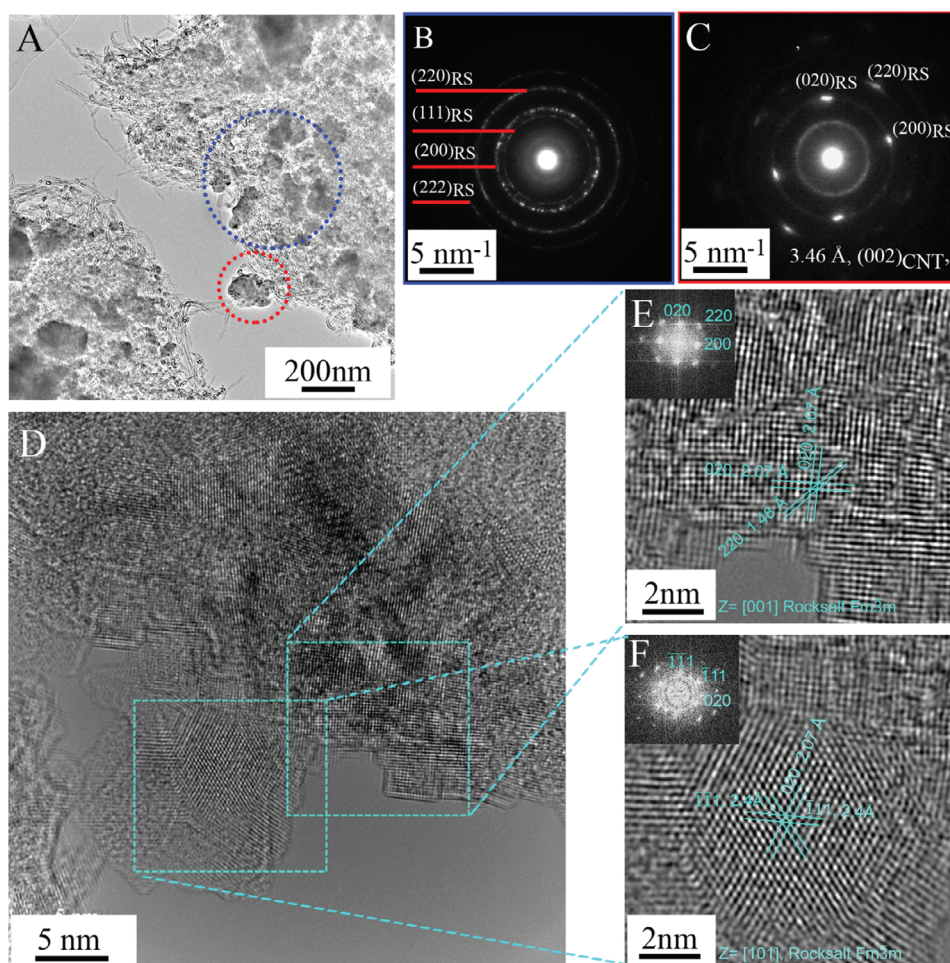

Figure 7. TEM data collected from the DOE10 sample prior to cycling. A) Bright-field image showing a mixture of DRX particles and carbon nanotubes. B,C) Electron diffraction patterns of the areas highlighted in blue and red in panel (A). D) HRTEM image and E,F) magnified views and (insets) corresponding FFTs of the areas denoted by the squares.
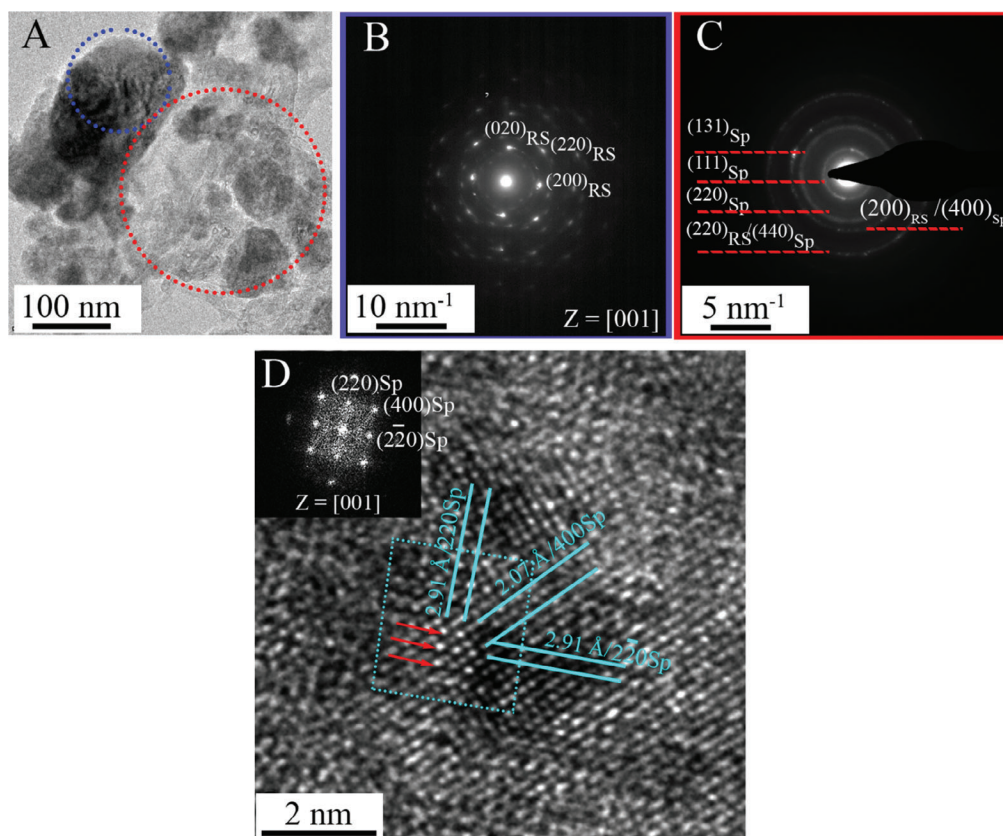
ADVANCED
SCIENCE NEWS

www.advancedsciencenews.com

ADVANCED
SUSTAINABLE
SYSTEMS

www.advsustainsys.com

Figure 8. TEM data collected from the DOE10 sample after 200 cycles at C/3 rate. A) Bright-field image. B,C) Electron diffraction patterns of the areas highlighted in blue and red in panel (A). D) HRTEM image of a particle along the [001] zone axis and (inset) corresponding FFT pattern confirming the presence of a spinel phase with space group $Fd-3m$.

Overall, our findings emphasize the importance of optimizing key parameters, such as the type and content of conductive additive, for improving cell cyclability. Nevertheless, the elevated carbon content utilized suggests that the diminished electronic conductivity persists as a limitation of DRX cathodes for battery implementation. Future research should focus both on addressing this issue and on elucidating the underlying redox mechanism(s).

In conclusion, our integrated approach of facile solid-state synthesis and DOE is effective in developing high-performance DRX materials for application in next-generation Li-ion cells.

Supporting Information

Supporting Information is available from the Wiley Online Library or from the author.

Acknowledgements

Conflict of Interest

A patent was filed for some of this work through BASF SE and the Karlsruher Institut für Technologie (KIT).

Data Availability Statement

The data that support the findings of this study are available from the corresponding author upon reasonable request.

Keywords

[1] A. Manthiram, *Nat. Commun.* **2020**, *11*, 1550.

[2] J. Lee, D. A. Kitchaev, D.-H. Kwon, C.-W. Lee, J. K. Papp, Y.-S. Liu, Z. Lun, R. J. Clément, T. Shi, B. D. McCloskey, J. Guo, M. Balasubramanian, G. Ceder, *Nature* **2018**, *556*, 185.

[3] Z. Lun, B. Ouyang, Z. Cai, R. J. Clément, D.-H. Kwon, J. Huang, J. K. Papp, M. Balasubramanian, Y. Tian, B. D. McCloskey, H. Ji, H. Kim, D. A. Kitchaev, G. Ceder, *Chem* **2020**, *6*, 153.

[4] D. A. Kitchaev, Z. Lun, W. D. Richards, H. Ji, R. J. Clément, M. Balasubramanian, D.-H. Kwon, K. Dai, J. K. Papp, T. Lei, B. D. McCloskey, W. Yang, J. Lee, G. Ceder, *Energy Environ. Sci.* **2018**, *11*, 2159.

[5] J. Lee, A. Urban, X. Li, D. Su, G. Hautier, G. Ceder, *Science* **2014**, *343*, 519.

[6] A. Urban, J. Lee, G. Ceder, *Adv. Energy Mater.* **2014**, *4*, 1400478.

[7] R. J. Clément, Z. Lun, G. Ceder, *Energy Environ. Sci.* **2020**, *13*, 345.

[8] D. Chen, J. Ahn, G. Chen, *ACS Energy Lett.* **2021**, *6*, 1358.

[9] W. Tang, A. Li, G. Zhou, Z. Chen, Z. Yang, J. Su, W. Zhang, *ACS Appl. Mater. Interfaces* **2022**, *14*, 38865.

[10] D. Chen, J. Wu, J. K. Papp, B. D. McCloskey, W. Yang, G. Chen, *Small* **2020**, *16*, 2000656.

[11] A. Urban, A. Abdellahi, S. Dacek, N. Artrith, G. Ceder, *Phys. Rev. Lett.* **2017**, *119*, 176402.

[12] N. Yabuuchi, M. Takeuchi, M. Nakayama, H. Shiiba, M. Ogawa, K. Nakayama, T. Ohta, D. Endo, T. Ozaki, T. Inamasu, K. Sato, S. Komaba, *Proc. Natl. Acad. Sci. USA* **2015**, *112*, 7650.

[13] J. Lee, D.-H. Seo, M. Balasubramanian, N. Twu, X. Li, G. Ceder, *Energy Environ. Sci.* **2015**, *8*, 3255.

[14] N. Yabuuchi, M. Nakayama, M. Takeuchi, S. Komaba, Y. Hashimoto, T. Mukai, H. Shiiba, K. Sato, Y. Kobayashi, A. Nakao, M. Yonemura, K. Yamanaka, K. Mitsuhara, T. Ohta, *Nat. Commun.* **2016**, *7*, 13814.

[15] H. Ji, A. Urban, D. A. Kitchaev, D.-H. Kwon, N. Artrith, C. Ophus, W. Huang, Z. Cai, T. Shi, J. C. Kim, H. Kim, G. Ceder, *Nat. Commun.* **2019**, *10*, 592.

[16] R. J. Clément, D. Kitchaev, J. Lee, G. Ceder, *Chem. Mater.* **2018**, *30*, 6945.

[17] Y. Sun, S. Jiao, J. Wang, Y. Zhang, J. Liu, X. Wang, L. Kang, X. Yu, H. Li, L. Chen, X. Huang, *J. Am. Chem. Soc.* **2023**, *145*, 11717.

[18] L. Li, B. Ouyang, Z. Lun, H. Huo, D. Chen, Y. Yue, C. Ophus, W. Tong, G. Chen, G. Ceder, C. Wang, *Nat. Commun* **2023**, *14*, 7448.

[19] S. Jiao, Y. Sun, D. Shi, Y. Zhang, X. Wang, J. Liu, L. Kang, F. Wang, X. Yu, H. Li, L. Chen, X. Huang, *Energy Environ. Sci.* **2024**, *17*, 4977.

[20] Y. Wang, Z. Wu, F. M. Azad, Y. Zhu, L. Wang, C. J. Hawker, A. K. Whittaker, M. Forsyth, C. Zhang, *Nat. Rev. Mater.* **2024**, *9*, 119.

[21] *PFAS Restriction Proposal, RECHARGE Statement for 2 Nd Call for Evidence-October* **2021**. https://rechargebatteries.org/wp-content/uploads/2022/09/Call-for-Evidence_RECHARGE-_-PFAS-restriction-V1.pdf (accessed November 2024)

[22] R. Lohmann, I. T. Cousins, J. C. DeWitt, J. Glüge, G. Goldenman, D. Herzke, A. B. Lindstrom, M. F. Miller, C. A. Ng, S. Patton, M. Scheringer, X. Trier, Z. Wang, *Environ. Sci. Technol.* **2020**, *54*, 12820.

[23] J. Lee, J. K. Papp, R. J. Clément, S. Sallis, D.-H. Kwon, T. Shi, W. Yang, B. D. McCloskey, G. Ceder, *Nat. Commun.* **2017**, *8*, 981.

[24] N. Takeda, S. Hoshino, L. Xie, S. Chen, I. Ikeuchi, R. Natsui, K. Nakura, N. Yabuuchi, *J. Power Sources* **2017**, *367*, 122.

[25] Z. Lun, B. Ouyang, D. A. Kitchaev, R. J. Clément, J. K. Papp, M. Balasubramanian, Y. Tian, T. Lei, T. Shi, B. D. McCloskey, J. Lee, G. Ceder, *Adv. Energy Mater.* **2019**, *9*, 1802959.

[26] M. Freire, N. V. Kosova, C. Jordy, D. Chateigner, O. I. Lebedev, A. Maignan, V. Pralong, *Nat. Mater.* **2016**, *15*, 173.

[27] J. Reed, G. Ceder, *Electrochem. Solid-State Lett.* **2002**, *5*, A145.

[28] J. Reed, G. Ceder, *Chem. Rev.* **2004**, *104*, 4513.

[29] Y. Huang, Y. Dong, S. Li, J. Lee, C. Wang, Z. Zhu, W. Xue, Y. Li, J. Li, *Adv. Energy Mater.* **2021**, *11*, 2000997.

[30] A. Urban, I. Matts, A. Abdellahi, G. Ceder, *Adv. Energy Mater.* **2016**, *6*, 1600488.

[31] M. A. Jones, P. J. Reeves, I. D. Seymour, M. J. Cliffe, S. E. Dutton, C. P. Grey, *Chem. Commun.* **2019**, *55*, 9027.

[32] W. H. Kan, B. Deng, Y. Xu, A. K. Shukla, T. Bo, S. Zhang, J. Liu, P. Pianetta, B.-T. Wang, Y. Liu, G. Chen, *Chem* **2018**, *4*, 2108.

[33] S. S. Zhang, *J. Energy Chem.* **2020**, *41*, 135.

[34] M. Küzma, R. Dominko, A. Meden, D. Makovec, M. Bele, J. Jamnik, M. Gaberšček, *J. Power Sources* **2009**, *189*, 81.

[35] R. Dominko, C. Vidal-Abraca Garrido, M. Bele, M. Kuezma, I. Arcon, M. Gaberscek, *J. Power Sources* **2011**, *196*, 6856.

[36] M. Yang, X. Zhao, C. Yao, Y. Kong, L. Ma, X. Shen, *Mater. Technol.* **2016**, *31*, 537.

[37] Y. Zhang, A. Hu, J. Liu, Z. Xu, L. Mu, S. Sainio, D. Nordlund, L. Li, C.-J. Sun, X. Xiao, Y. Liu, F. Lin, *Adv. Funct. Mater.* **2022**, *32*, 2110502.

[38] B. Marinho, M. Ghislandi, E. Tkalya, C. E. Koning, G. de With, *Powder Technol.* **2012**, *221*, 351.

[39] D.-H. Kwon, J. Lee, N. Artrith, H. Kim, L. Wu, Z. Lun, Y. Tian, Y. Zhu, G. Ceder, *Cell Rep. Phys. Sci.* **2020**, *1*, 100187.

[40] Z. Cai, B. Ouyang, H.-M. Hau, T. Chen, R. Giovine, K. P. Koirala, L. Li, H. Ji, Y. Ha, Y. Sun, J. Huang, Y. Chen, V. Wu, W. Yang, C. Wang, R. J. Clément, Z. Lun, G. Ceder, *Nat. Energy* **2024**, *9*, 27.

[41] M. Luo, S. Zheng, J. Wu, K. Zhou, W. Zuo, M. Feng, H. He, R. Liu, J. Zhu, G. Zhao, S. Chen, W. Yang, Z. Peng, Q. Wu, Y. Yang, *J. Mater. Chem. A* **2020**, *8*, 5115.

[42] D. Chen, W. H. Kan, G. Chen, *Adv. Energy Mater.* **2019**, *9*, 1901255.

[43] T. Li, T. S. Geraci, K. P. Koirala, A. Zohar, E. N. Bassey, P. A. Chater, C. Wang, A. Navrotsky, R. J. Clément, *J. Am. Chem. Soc.* **2024**, *146*, 24296.

[44] J. Ahn, Y. Ha, R. Satish, R. Giovine, L. Li, J. Liu, C. Wang, R. J. Clement, R. Kostecki, W. Yang, G. Chen, *Adv. Energy Mater.* **2022**, *12*, 2200426.

[45] J. Ahn, R. Giovine, V. C. Wu, K. P. Koirala, C. Wang, R. J. Clément, G. Chen, *Adv. Energy Mater.* **2023**, *13*, 2300221.